

Emergent climate change patterns originating from deep ocean warming in climate mitigation scenarios

Received: 23 January 2023

Ji-Hoon Oh¹, Jong-Seong Kug^{1,2}✉, Soon-Il An^{1,3}, Fei-Fei Jin^{1,4}, Michael J. McPhaden⁵ & Jongsoo Shin^{1,6}

Accepted: 5 January 2024

Published online: 1 February 2024

 Check for updates

The global oceans absorb most of the surplus heat from anthropogenic warming, but it is unclear how this heat accumulation will affect the Earth's climate under climate mitigation scenarios. Here we show that this stored heat will be released at a much slower rate than its accumulation, resulting in a robust pattern of surface ocean warming and consequent regional precipitation. The surface ocean warming is pronounced over subpolar to polar regions and the equatorial eastern Pacific where oceans are weakly stratified to allow vigorous heat release from the deep ocean to the surface layer. We also demonstrate that this ocean warming pattern largely explains changes in the precipitation pattern, including the southward shift of the Intertropical Convergence Zone and more moistening in high latitudes. This study suggests that deep ocean warming may hinder climate recovery in some regions, even if carbon neutrality or net negative emissions are successfully achieved.

The ocean, covering more than 70% of Earth's surface, exerts a critical role in regulating the climate system. It has absorbed more than 90% of the current energy imbalance (surplus heat) caused by persistent emissions of anthropogenic greenhouse gases (GHGs), particularly carbon dioxide (CO_2)^{1–3}; thus, the ocean plays a role in slowing down global surface warming. Indeed, a global warming hiatus from 2002 to 2012⁴ was associated with enhanced subsurface ocean heat uptake in the equatorial Pacific^{5,6}. Widespread and substantial ocean warming has been observed since the 1950s and continues to accelerate^{7,8}.

A key characteristic of ocean warming is the various response timescales of different ocean depths to climate forcings. The ocean mixed layer responds rapidly to surface heating due to direct interaction with the atmosphere, while the deeper ocean adjusts much more slowly due to its larger thermal inertia and the slow heat transport into it⁹. As a result, deep ocean warming is expected to persist for

centuries even after achieving net-zero CO_2 emissions^{10,11}. In other words, today's GHG emissions will have enduring impacts on future ocean changes, giving a long-term memory to our climate system in response to anthropogenic forcing.

Under the potential threats from anthropogenic climate change, a worldwide commitment has been pledged to limit global warming to below 2 °C and preferably to 1.5 °C, as codified in the 2015 Paris Agreement. This goal requires immediate and decisive international action to achieve net-zero and negative CO_2 emissions^{12–15}, not only by reducing anthropogenic CO_2 emissions, but also by artificial techniques to remove CO_2 from the atmosphere. This crucial step is essential to restore the climate system and ensure a sustainable future. Accordingly, recent studies have investigated the hysteresis and reversibility of global or regional climate in response to atmospheric CO_2 removal by using idealized climate model experiments^{16–33}. Global total ocean heat

¹Division of Environmental Science and Engineering, Pohang University of Science and Technology (POSTECH), Pohang, South Korea. ²Institute for Convergence Research and Education in Advanced Technology, Yonsei University, Seoul, South Korea. ³Department of Atmospheric Sciences/ Irreversible Climate Change Research Center, Yonsei University, Seoul, South Korea. ⁴Department of Atmospheric Sciences, University of Hawaii, Honolulu, HI, USA. ⁵NOAA/Pacific Marine Environmental Laboratory, Seattle, WA, USA. ⁶Woods Hole Oceanographic Institution, Woods Hole, Falmouth, MA, USA. ✉e-mail: jskug1@gmail.com

content (OHC) and the resultant thermosteric sea level rise associated with the slow response of the deep ocean have exhibited the clearest irreversible response across the different climate models despite the rapid CO₂ removal (for example, 1% yr⁻¹ or even 5% yr⁻¹) to the present level^{21–23}. To avoid ambiguity, the term ‘irreversible change’ here is used as a long-term transient recovery on a multicentury timescale (more than 200 yr) that is humanly perceptible after the CO₂ concentration returns to baseline.

Such an irreversible response of ocean warming as a result of past anthropogenic GHG emissions may modulate global or regional surface climate^{9,34–37} in addition to changes in sea level and the marine environment itself. From a global perspective, the sole way to diminish the heat absorbed by the ocean from the atmosphere is to release it back into the atmosphere. For example, the deeper ocean may gradually transport stored heat to the upper ocean and mixed layers, ultimately being released back into the atmosphere. This potential long-term counteractive effect of the ocean as a heat source for the surface climate system can persist over centuries. Hence, there is a possibility that the ocean’s thermal inertia may affect the surface climate system in terms of both timescale and regional pattern. Analysing this aspect can provide vital information for regional climate adaptation and mitigation strategies from a long-term perspective. Despite this importance in the long-term perspective, an active role of the deep ocean as a heat source for the surface climate has often been overlooked, mainly due to its predominant recognition as a thermal buffer. This perspective stems from the dominance of radiative forcing caused by the rapid increases in GHGs. However, the counteractive effect of the ocean will be clearer under a net negative CO₂ emission scenario, owing to the discrepancy in adjustment timescale between the surface and deep ocean in response to CO₂ removal.

Here we mainly explore the active role of deep ocean warming on the surface climate. To address this scientific question, a large ensemble experiment is performed by employing the Community Earth System Model (CESM) with 28 ensemble members. In this experiment, the atmospheric CO₂ concentration increases by 1% yr⁻¹ for 140 yr until it quadruples (ramp-up), then declines symmetrically to the initial CO₂ level (ramp-down) and is held constant for 220 yr thereafter (restoring, see Methods for details).

Irreversible response of deep ocean warming

In response to CO₂ forcing, the global total (global and full-depth integrated) OHC clearly exhibits an irreversible change (Fig. 1a,b). After ~85 yr (year 2235) from the CO₂ peak, the global total OHC anomaly reaches the maximum (~4.3 × 10²⁴ J), which corresponds to ~60 cm rise in global thermosteric sea level. It then begins to decrease slowly but still represents ~62% of the maximum at the end of the simulation even after ~200 yr since the CO₂ level has returned to the present climate level, indicating an irreversible change on a human timescale. This suggests that even if the initial CO₂ level is fully restored, the fingerprint of past global warming remains in the global ocean in the form of massive heat. Indeed, the temporal evolution of the total OHC is almost identical to the accumulated surface heat flux from the atmosphere, confirming a heat balance between the ocean and the atmosphere (Fig. 1a).

The irreversible response of ocean warming is associated with the slow response of the deep ocean^{9,10,23,35}. Here, the below 700 m oceans is defined as the ‘deep ocean’ on the basis of the climatological global pycnocline depth, which is found at ~700 m^{38,39} (varying from 500 to 1,000 m), and the observation that much of modern ocean warming is in the upper 700 m⁸. Indeed, the temperature response to radiative forcing is more delayed with depth (Fig. 1b). The ocean temperature in the upper 700 m begins to decrease during the ramp-down period, while the temperature between 700 m and 2,000 m continues to increase until the onset of the restoring period, so that, at this time, the maximum temperature anomaly occurs at ~700 m. However, water below 2,000 m exhibits a slow and sustained increase in temperature

since this layer is still adjusting to the past increased atmospheric CO₂ concentration. Thus, the overall temporal evolution of total OHC is largely explained by OHC above 2,000 m (Fig. 1b). In addition, to examine the spatial pattern of irreversible OHC response, the total OHC distribution (Fig. 1c) is averaged over the last 100 yr of the simulation (light blue box in Fig. 1a). It exhibits overall positive signals across the globe but is especially pronounced in the Atlantic and the Southern Ocean due to previous active local ocean heat uptake (OHU, downward net surface heat flux) and its redistribution by the meridional overturning circulation^{8,40–43} (Fig. 1c).

An important feature is that the global total OHC begins to slowly decrease in accordance with the rapid reduction and subsequent stabilization of atmospheric CO₂ concentration, even if there is a delay of decades after the CO₂ peak (Fig. 1a). This loss of total OHC is primarily attributed to loss in the upper 2,000 m (Fig. 1b). Since the sign of global OHU changes from positive to negative around year 2235 (maximum of global total OHC), the global total OHC begins to decrease. This corresponds to a net heat loss to the atmosphere across the sea surface, which implies a net transition in the role of the ocean from a heat sink to a heat source for the atmosphere. This may hinder the recovery of surface climate by continuous heat supply, which can eventually contribute to the hysteresis and irreversibility of global or regional climate.

Spatial patterns of irreversible surface climate changes

To explore the ocean warming-induced irreversible pattern of surface climate, here the irreversible change and its pattern are defined as the difference between the time average of the last 100 yr (years 2401–2500) of the simulation and the 900-yr mean of the present-day control simulation (see Methods). The irreversible pattern of sea surface temperature (SST) shows overall positive signals, indicating that the SST remains higher than in the present climate. Notably, the SST pattern exhibits distinct delayed responses over the subpolar regions such as the Southern Ocean (SO), subpolar North Atlantic (SPNA) and Bering Sea (BS). An El Niño-like pattern is also evident in the equatorial eastern Pacific (EEP) (Fig. 2a). This spatial pattern is similar to the slow response to global warming reported in the literature^{9,34,36,44}, which is partially obscured by the fast-varying surface warming pattern. The long-lasting and specific SST pattern is hypothesized to be associated with irreversible ocean warming, leading to the natural interest in understanding their dynamic connection.

Next, the patterns of total OHC and SST over the last 100 yr of the simulation are compared to examine the linkage between them. It is evident that the SST pattern (Fig. 2a) does not correspond to that of total OHC (Fig. 1c), indicating that the local OHC response is not directly linked to local SST. That is, even if a larger amount of heat remains in a water column, it is not directly connected to higher SST. A plausible explanation for the irreversible SST pattern could be related to spatial distribution in the background ocean stratification. This distribution can roughly indicate how effectively properties and tracers such as carbon and heat in the deeper ocean are ventilated into the upper ocean. Indeed, recent studies have reported that the climatological ocean circulation and stratification are strongly related to the future heat and carbon uptake⁴⁵, and the distribution of their storage⁴⁶.

It is hypothesized that background ocean stratification might be a key factor for the linkage between the irreversible patterns of OHC and SST. Ocean stratification is roughly represented by the squared buoyancy frequency (N^2) averaged over the upper 2,000 m (Fig. 2b) where OHU occurs (Fig. 1b). The N^2 is positive because the density increases with depth. Oceans with a smaller N^2 exhibit lower static stability, characterized by relatively stronger residual upwelling of dense deep water or vertical mixing that occurs both along and across isopycnals. These processes weaken the vertical density gradient in the water column. Therefore, it is possible that in oceans with smaller N^2 , the accumulated heat in deeper depths can be more efficiently

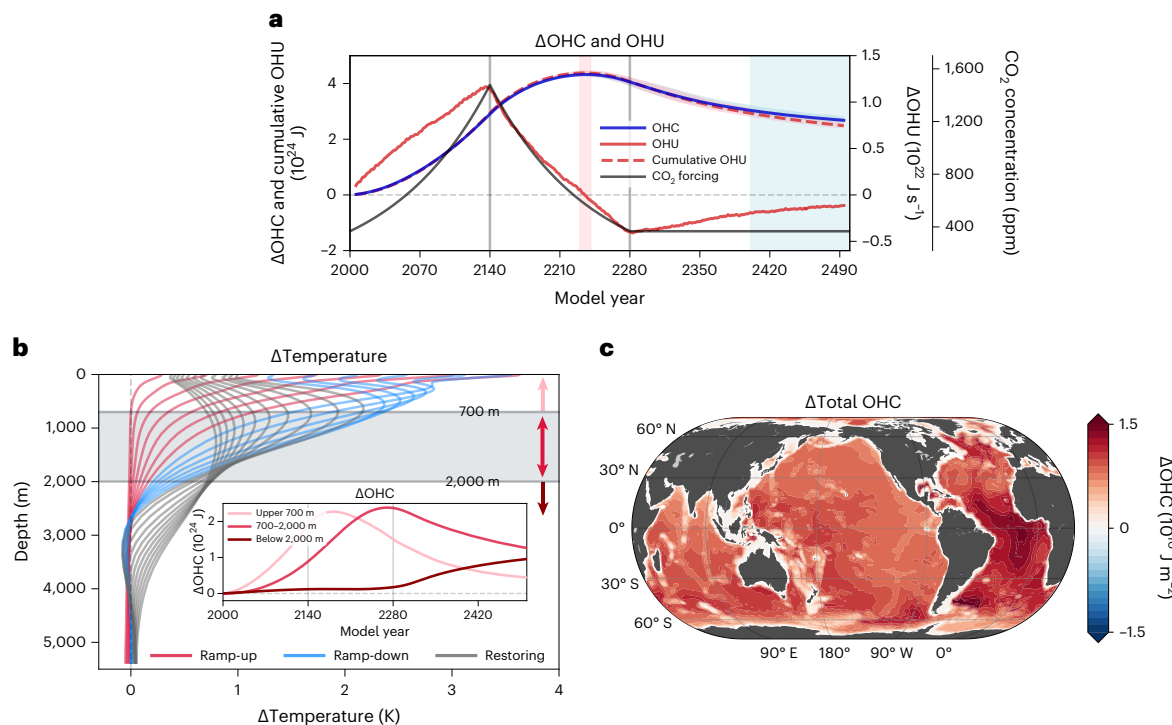


Fig. 1 | Temporal evolution and spatial pattern of ocean warming. **a**, Temporal evolution of applied CO₂ concentration forcing (black, 2nd right y-axis), ensemble mean of the global total (global and full-depth integrated) OHC (blue, left y-axis), OHU (that is, net surface heat flux, red, 1st right y-axis) and cumulative (time-integrated) OHU (dotted red, left y-axis). Lines and light shadings indicate 28 ensemble means and full ensemble spread, respectively. The light red and blue boxes indicate the year 2235 (OHC peak phase) and the last 100 yr of the simulation, respectively. **b**, Temporal evolution of the vertical profile of the

global mean ocean temperature every 20 yr. The red, blue and grey line colours represent the ramp-up, -down and restoring periods, respectively. Inset: the temporal evolution of the globally and vertically integrated ensemble mean OHC. The light red, red and dark red colours represent the 0–700 m, 700–2,000 m and below 2,000 m integration, respectively. All time series are based on annual means relative to year 2000 and smoothed by an 11-yr running mean. **c**, Total OHC anomaly averaged over the last 100 yr (year 2401–2500) relative to year 2000. Only values significant at the 95% confidence level are shown.

ventilated. Indeed, the spatial pattern of the background N^2 shows some similarity to the irreversible SST pattern (Fig. 2a,c), although the detailed regional patterns are different. In particular, weakly stratified background conditions are found in areas of apparent SST irreversibility, such as the SO, SPNA, BS and EEP.

More specifically, vigorous wind-driven upwelling, as measured by Eulerian vertical velocity (W_{Eulerian}), is observed in the subpolar gyre and equatorial ocean as well as south of the Antarctic Circumpolar Current (ACC) including in the SO, SPNA, BS and EEP (Extended Data Fig. 1). These intense upward motions extend coherently to depths of at least 1,000 m and are partially offset by mesoscale eddy-induced vertical velocity ($W_{\text{eddy-induced}}$, that is, bolus velocity) parameterized following ref. 47 (Extended Data Fig. 2). Consequently, the resulting residual upwelling ($W_{\text{residual}} = W_{\text{Eulerian}} + W_{\text{eddy-induced}}$) can effectively transport heat from the deeper layer to the mixed layer along the sloped isopycnals (Fig. 2c). In regions where the winter mixed layer is deep, the heat can be effectively supplied to the surface. Notably, in the Labrador Sea, located in the SPNA, there is a particularly strong process for efficiently mixing up the heat deposited at depths of up to ~2,000 m (light pink and blue shadings in Fig. 2c and Extended Data Fig. 3a). The enhanced meridional oceanic heat transport due to the overshoot of the Atlantic Meridional Overturning Circulation (AMOC, Extended Data Fig. 4)^{18,48} also plays a role in the distinct SST irreversibility in the SPNA. Furthermore, the mesoscale eddy-induced mixing along the tilted isopycnals, which is parameterized by the diffusion operator with isopycnal diffusivity following ref. 49 (Extended Data Fig. 3b), contributes to the heat exchanges between the deeper and surface layers.

In summary, the heat accumulated in the deep ocean by global warming is effectively ventilated in specific regions through the

vigorous residual upwelling and isopycnal and diapycnal mixing processes, facilitating active heat exchanges there and ultimately delaying SST recovery. In addition, once the heat is released to the surface, strong positive feedback⁵⁰ such as sea ice–albedo and low cloud–SST feedback^{51,52} (Extended Data Fig. 5) further amplify the warming by increasing downward solar radiation over the subpolar to polar areas and along the west coast of the continent (for example, sea ice and low cloud reduction patterns in Extended Data Fig. 5). This complex interplay of both oceanic upward heat transfer and atmospheric positive feedback eventually shapes the detailed long-lasting SST pattern as a result of irreversible ocean warming. Considerable deep ocean warming is prevalent over the whole global ocean even at the end of the simulation. Hence, the irreversible SST pattern is largely explained by local ocean ventilation in the background state regardless of the horizontal distribution of the OHC anomaly.

In addition, such an SST pattern plays a role in shaping the irreversible pattern of the hydrological cycle. Due to the higher SST than in the present climate across the globe (Fig. 2a), precipitation responses are also enhanced overall (Fig. 2d). For example, there are distinct precipitation increases over the SO and SPNA, consistent with the regions where the SST increases are the strongest. The most pronounced feature of the precipitation response is the southward shift of the Intertropical Convergence Zone (ITCZ) in the Pacific and Atlantic Oceans, characterized by a rainfall decrease along the climatological ITCZ and an increase south of that. This feature is also closely related to the SST pattern. According to the energetic framework, the latitudinal position of the ITCZ is associated with cross-equatorial energy transport regulated by meridional energy exchanges between the hemispheres^{53–56}. Therefore, widespread warming in the SO can pull the ITCZ to the south

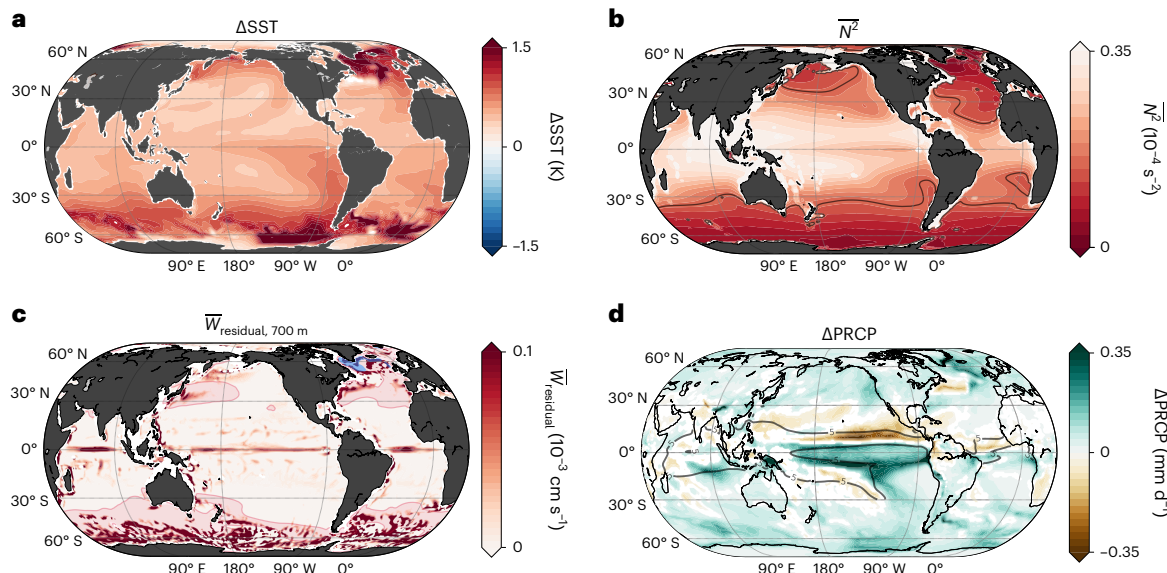


Fig. 2 | Spatial patterns of irreversible surface climate changes. **a,d**, As in Fig. 1c, but for the SST (a) and precipitation (PRCP) (d). The grey contour line in **d** denotes the background annual ocean precipitation of 5 mm d⁻¹ within 30° S–30° N. **b**, Background upper 2,000 m averaged squared buoyancy frequency (N^2). The grey contour line in **b** is the background N^2 of $0.15 \times 10^{-4} \text{ s}^{-2}$. Note that the order of the colours in **b** is in reverse. **c**, Background residual (sum of Eulerian and bolus vertical velocities) ocean vertical velocity (W_{residual}) at

700 m. Only upwelling regions are displayed to highlight the result. The light pink and blue shadings denote areas where the maximum background mixed layer depth (monthly maximum among 12 months climatology in each grid) exceeds 150 m and 700 m, respectively. Here, the ‘background’ (overbar) refers to the long-term mean of each physical quantity in the present-day control simulation (year 2000 level).

by weakening the poleward atmospheric energy transport from the tropics to the extratropics in the Southern Hemisphere²⁷. Moreover, the El Niño-like SST pattern also leads to a local ITCZ shift to the south⁵⁷, which further enhances the precipitation response in the EEP; this tropical rainfall variation may affect the formation of the extratropical rainfall pattern via atmospheric teleconnections⁵⁸. On the basis of this dynamical relationship between the SST and precipitation patterns, we highlight here that the horizontal distribution of the background ocean stratification is also important in shaping the irreversible pattern of the hydrological cycle as well as that of temperature. In addition, CMIP6 models and the inter-ensemble relationship further support our argument (Extended Data Fig. 6–8 and Supplementary Figs. 1–3).

Evidence from initial warming experiments

So far, it is suggested that the irreversible SST pattern is determined by the slow ocean warming and the climatological distribution of the ocean stratification. However, surface climate changes in the coupled climate system are highly complex since they are influenced by various factors and feedback (such as sea ice–albedo or low cloud–SST feedback, Extended Data Fig. 5) in addition to the vertical heat exchanges. Therefore, one should be careful to conclude solely from statistical analysis and spatial similarity that the irreversible patterns of surface temperature and hydrological cycles indeed originate from deep ocean warming.

To supplement our arguments, four additional initial warming experiments (named IW_whole, IW_be100, IW_be700 and IW_ab100) are conducted to explore the intrinsic role of stored heat in the deep ocean in shaping a particular surface climate pattern. All initial warming experiments are integrated with constant atmospheric CO₂ concentration, but spatially uniform temperature and salinity perturbation profiles were added to the ocean’s initial condition (see Methods). That is, the initial temperature and salinity perturbations are entirely identical across all ocean grids. The added initial perturbations are the vertical profile of the global mean temperature and salinity at the year 2280 when the CO₂ concentration first return to the year 2000 level

(Fig. 3a). Specifically, to isolate the effect of the deep ocean, the initial warming is added to the whole depth, below 100 m depth, below 700 m depth and above 100 m depth in the IW_whole, IW_be100, IW_be700 and IW_ab100, respectively. By investigating how this uniform initial warming emerges to the surface, we find that the background local ocean stratification is an important factor in the irreversible SST pattern as a bridge between the deep ocean and the surface.

When the initial warming is given in the upper 100 m (IW_ab100), the immediate global mean SST (GMST) increase rapidly decays due to the intense heat release into the atmosphere. However, in the presence of deep ocean warming, the GMST gradually increases up to ~1.2 K (IW_whole and IW_be100) and 0.6 K (IW_be700) (Fig. 3b) and then slowly decays. This implies that the cumulative heat in the deep ocean is still capable of considerably raising GMST, even though atmospheric CO₂ concentrations have totally returned to the present level. This slow process can induce irreversible behaviour in the surface climate system. Compared with the IW_whole and IW_be100, the GMST in the IW_be700 slowly evolves and becomes close to that of IW_whole during the last 50 yr despite the smaller total heat of initial thermal perturbation than that of the IW_whole. It is worth noting that GMST in the three IW_EXPs with deep ocean warming gradually decreases but is still not totally back to the initial level for at least 150 yr.

More importantly, we found that the three experiments (IW_whole, IW_be100 and IW_be700) reveal quite similar SST and precipitation patterns in the last 50 yr, suggesting that uniform deep ocean warming tends to have a particular horizontal pattern of the surface climate. Strikingly, the spatial patterns of both SST and precipitation in the three IW_EXPs are highly similar to those of the irreversible patterns shown in Fig. 2, with significant spatial correlation coefficients of 0.94, 0.95, 0.92 (SST), and 0.91, 0.92, 0.90 (precipitation) in the IW_whole, IW_be100 and the IW_be700, respectively (Fig. 3c,d and Extended Data Fig. 9). In addition to the SST pattern, a high spatial resemblance is also observed in the land surface temperature (Extended Data Fig. 10). This spatial similarity despite a uniform deep ocean warming clearly demonstrates that the combination of deep ocean warming and the

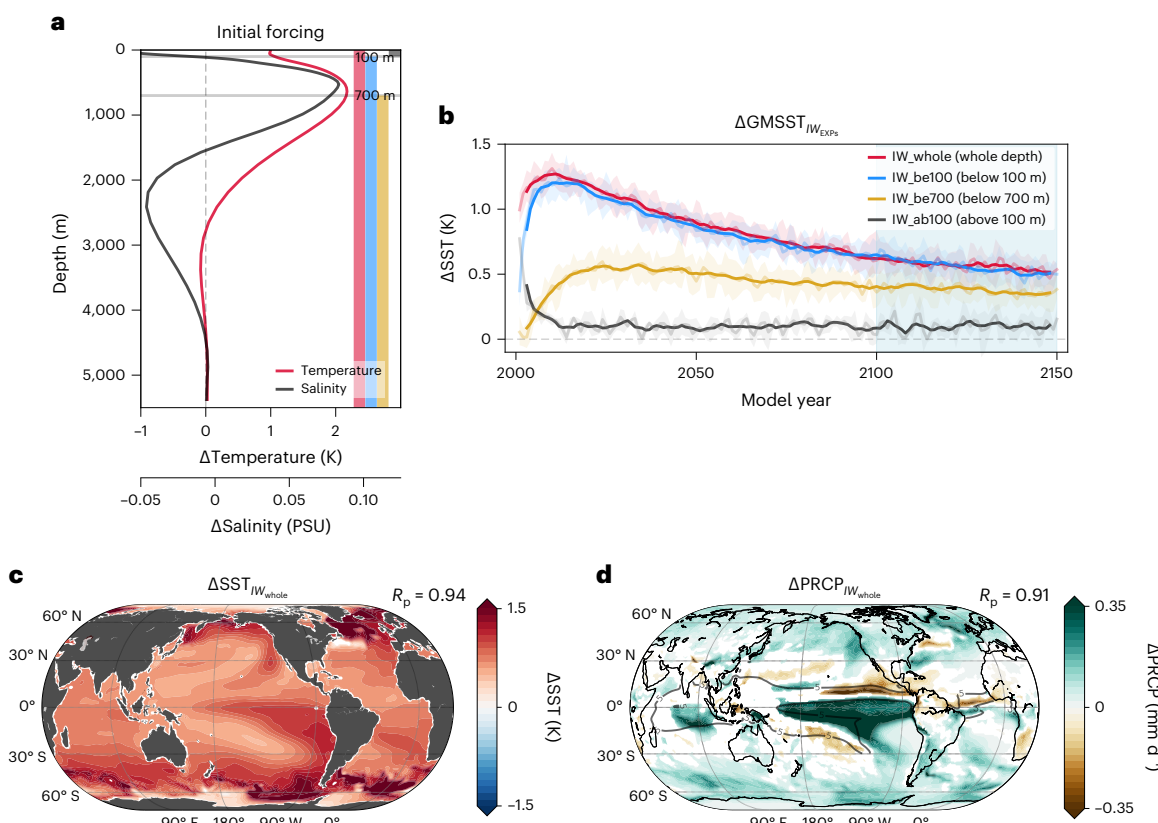


Fig. 3 | Design and results of the initial warming experiment. **a**, Global mean potential temperature (red) and salinity (black) profile in year 2280 when the CO₂ concentration first returns to the present level. These two vertical profiles are uniformly added to all ocean grids of the model's original initial condition (year 2000 condition). The two grey horizontal lines denote the 100 m and 700 m depths, respectively. The red, blue, yellow and black vertical bars indicate the depth of the initial forcing used in each experiment (see Methods for a detailed description of the initial warming experiment). **b**, Temporal evolution of the ensemble mean of the global mean SST of IW_{whole} (red), IW_{be100} (blue),

IW_{be700} (yellow) and IW_{ab100} (black) relative to the year 2000. The light and solid lines denote yearly evolutions and evolutions after being smoothed by a 5-yr running mean, respectively. **c,d**, SST and precipitation anomalies averaged over the last 50 yr (2101–2150) of IW_{whole} relative to year 2000. The grey contour line in **d** denotes the climatological annual mean ocean precipitation of 5 mm d⁻¹ within 30° S–30° N. In **c** and **d**, only significant values at the 95% confidence level are shown; the numbers labelled at the top right corner are the pattern correlations between each panel's pattern and the reference irreversible SST and PRCP patterns (Fig. 2a and d).

local distribution of the background stratification shaped by vertical upwelling and mixing is a key factor in shaping the irreversible surface climate changes.

One may argue that the irreversible SST pattern could be mainly shaped by the strong positive feedback in the subpolar to polar areas, not by local ocean stratification. However, when the initial warming is only added to the surface layer (~100 m, IW_{ab100}), the spatial patterns of SST, precipitation and land surface temperature exhibit no consistency with the patterns in Fig. 2 (Extended Data Figs. 9e,f and 10e). These results imply that although various factors contribute to the shape of surface climate, such as air-sea interaction, the fundamental cause of the irreversible pattern of surface climate originates from the release of deep ocean heat where vertical heat exchange is relatively vigorous.

Discussion

It has been well documented that the ocean plays a role in slowing down global surface warming by absorbing most of the Earth's radiative imbalance due to anthropogenic GHGs. However, it is demonstrated here that the accumulated heat in the deep ocean could bring about irreversible climate change by eventually releasing the heat into the atmosphere.^{9,33–35,37} In particular, the deep ocean warming-induced irreversible climate change produces a specific spatial pattern, which is closely related to climatological ocean stratification. Heat release from the deep ocean to the surface depends largely on the extent of

the global ocean stratification, thus it naturally takes a long time for heat to be transported to the surface given the strong background ocean stratification. In addition to this background stratification in the global ocean, positive local feedback exerts a role in slowing the heat release from deeper depths over the weakly stratified oceans. For example, the deep ocean-induced surface warming simultaneously accompanies local positive feedback³⁰ such as sea ice-albedo and low cloud-SST feedback^{52,59} (Extended Data Fig. 5), which can amplify or maintain the positive SST perturbation by minimizing outgoing surface heat flux towards the atmosphere. In other words, the heat loss into the atmosphere occurs inefficiently despite the considerable surface warming, thus the OHC loss evolves slowly, resulting in strong irreversible ocean warming (Fig. 1) and further irreversible surface climate changes (Fig. 2). A quantitative analysis of the role of these surface feedback in diminishing surface heat loss, and thereby strengthening the irreversibility of SST and deep ocean heat loss, should be addressed in a further study.

Even though this study focused on the irreversible response in the restoring period after the ramp-down scenario, the effect of deep ocean warming on the surface climate would always operate when considerable deep ocean warming exists. For example, even when we successfully achieve net-zero emissions, the deep ocean warming-induced climate patterns would emerge and impact the global climate. Therefore, how much and/or how long GHGs will be emitted until reaching net-zero

emissions will determine the amount of accumulated warming in the deep ocean, which will be a critical factor in determining the recovery of Earth's climate. In contrast, when the atmospheric CO₂ concentration is changing, whether increasing or decreasing, the effect of the deep ocean warming can be hidden in the patterns of fast responses to strong radiative forcing and associated complex feedback. However, the deep ocean warming definitely plays a role in our climate system and its impacts will be stronger and sustained longer if the accumulated deep ocean warming is larger. Therefore, we still need to take into account the effect of the deep ocean-induced climate pattern for long-term climate projections.

Online content

Any methods, additional references, Nature Portfolio reporting summaries, source data, extended data, supplementary information, acknowledgements, peer review information; details of author contributions and competing interests; and statements of data and code availability are available at <https://doi.org/10.1038/s41558-024-01928-0>.

References

1. Meyssinac, B. et al. Measuring global ocean heat content to estimate the earth energy imbalance. *Front. Mar. Sci.* <https://doi.org/10.3389/fmars.2019.00432> (2019).
2. von Schuckmann, K. et al. Heat stored in the Earth system: where does the energy go? *Earth Syst. Sci. Data* **12**, 2013–2041 (2020).
3. Cheng, L. et al. Improved estimates of ocean heat content from 1960 to 2015. *Sci. Adv.* **3**, e1601545 (2017).
4. Easterling, D. R. & Wehner, M. F. Is the climate warming or cooling? *Geophys. Res. Lett.* **36**, L08706 (2009).
5. England, M. H. et al. Recent intensification of wind-driven circulation in the Pacific and the ongoing warming hiatus. *Nat. Clim. Change* **4**, 222–227 (2014).
6. Meehl, G. A., Arblaster, J. M., Fasullo, J. T., Hu, A. & Trenberth, K. E. Model-based evidence of deep-ocean heat uptake during surface-temperature hiatus periods. *Nat. Clim. Change* **1**, 360–364 (2011).
7. Cheng, L., Abraham, J., Hausfather, Z. & Trenberth, K. E. How fast are the oceans warming? *Science* **363**, 128–129 (2019).
8. Cheng, L. et al. Past and future ocean warming. *Nat. Rev. Earth Environ.* <https://doi.org/10.1038/s43017-022-00345-1> (2022).
9. Held, I. M. et al. Probing the fast and slow components of global warming by returning abruptly to preindustrial forcing. *J. Clim.* **23**, 2418–2427 (2010).
10. Solomon, S., Plattner, G.-K., Knutti, R. & Friedlingstein, P. Irreversible climate change due to carbon dioxide emissions. *Proc. Natl Acad. Sci. USA* **106**, 1704–1709 (2009).
11. Frölicher, T. L., Winton, M. & Sarmiento, J. L. Continued global warming after CO₂ emissions stoppage. *Nat. Clim. Change* **4**, 40–44 (2014).
12. Hoegh-Guldberg, O., Jacob, D. & Taylor, M. in *IPCC Special Report on Global Warming of 1.5 °C* (eds Masson-Delmotte, V. et al.) 175–181 (Cambridge Univ. Press, 2018).
13. Luderer, G. et al. Residual fossil CO₂ emissions in 1.5–2 °C pathways. *Nat. Clim. Change* **8**, 626–633 (2018).
14. Tong, D. et al. Committed emissions from existing energy infrastructure jeopardize 1.5 °C climate target. *Nature* **572**, 373–377 (2019).
15. Welsby, D., Price, J., Pye, S. & Edkins, P. Unextractable fossil fuels in a 1.5 °C world. *Nature* **597**, 230–234 (2021).
16. Boucher, O. et al. Reversibility in an Earth System model in response to CO₂ concentration changes. *Environ. Res. Lett.* **7**, 024013 (2012).
17. Garbe, J., Albrecht, T., Levermann, A., Donges, J. F. & Winkelmann, R. The hysteresis of the Antarctic ice sheet. *Nature* **585**, 538–544 (2020).
18. Jackson, L. C., Schaller, N., Smith, R. S., Palmer, M. D. & Vellinga, M. Response of the Atlantic meridional overturning circulation to a reversal of greenhouse gas increases. *Clim. Dyn.* **42**, 3323–3336 (2014).
19. Sgubin, G., Swingedouw, D., Drijfhout, S., Hagemann, S. & Robertson, E. Multimodel analysis on the response of the AMOC under an increase of radiative forcing and its symmetrical reversal. *Clim. Dyn.* **45**, 1429–1450 (2015).
20. Chadwick, R., Wu, P., Good, P. & Andrews, T. Asymmetries in tropical rainfall and circulation patterns in idealised CO₂ removal experiments. *Clim. Dyn.* **40**, 295–316 (2013).
21. Wu, P., Ridley, J., Pardaens, A., Levine, R. & Lowe, J. The reversibility of CO₂-induced climate change. *Clim. Dyn.* **45**, 745–754 (2015).
22. Bouttes, N., Gregory, J. M. & Lowe, J. A. The reversibility of sea level rise. *J. Clim.* **26**, 2502–2513 (2013).
23. Ehler, D. & Zickfeld, K. Irreversible ocean thermal expansion under carbon dioxide removal. *Earth Syst. Dyn.* **9**, 197–210 (2018).
24. Oh, J., An, S., Shin, J. & Kug, J. Centennial memory of the Arctic Ocean for future Arctic climate recovery in response to a carbon dioxide removal. *Earth Future* **10**, e2022EF002804 (2022).
25. An, S. et al. Global cooling hiatus driven by an AMOC overshoot in a carbon dioxide removal scenario. *Earth Future* **9**, e2021EF002165 (2021).
26. Song, S.-Y. et al. Asymmetrical response of summer rainfall in East Asia to CO₂ forcing. *Sci. Bull.* **67**, 213–222 (2022).
27. Kug, J.-S. et al. Hysteresis of the intertropical convergence zone to CO₂ forcing. *Nat. Clim. Change* **12**, 47–53 (2022).
28. Kim, S.-K. et al. Widespread irreversible changes in surface temperature and precipitation in response to CO₂ forcing. *Nat. Clim. Change* **12**, 834–840 (2022).
29. Pathirana, G. et al. Increase in convective extreme El Niño events in a CO₂ removal scenario. *Sci. Adv.* **9**, eadh2412 (2023).
30. Schwinger, J., Asaadi, A., Steinert, N. J. & Lee, H. Emit now, mitigate later? Earth system reversibility under overshoots of different magnitudes and durations. *Earth Syst. Dyn.* **13**, 1641–1665 (2022).
31. Li, X., Zickfeld, K., Mathesius, S., Kohfeld, K. & Matthews, J. B. R. Irreversibility of marine climate change impacts under carbon dioxide removal. *Geophys. Res. Lett.* **47**, e2020GL088507 (2020).
32. Mathesius, S., Hofmann, M., Caldeira, K. & Schellnhuber, H. J. Long-term response of oceans to CO₂ removal from the atmosphere. *Nat. Clim. Change* **5**, 1107–1113 (2015).
33. Wu, P., Wood, R., Ridley, J. & Lowe, J. Temporary acceleration of the hydrological cycle in response to a CO₂ rampdown. *Geophys. Res. Lett.* **37**, L12705 (2010).
34. Long, S.-M., Xie, S.-P., Zheng, X.-T. & Liu, Q. Fast and slow responses to global warming: sea surface temperature and precipitation patterns. *J. Clim.* **27**, 285–299 (2014).
35. Long, S. M. et al. Effects of ocean slow response under low warming targets. *J. Clim.* **33**, 477–496 (2020).
36. Xie, S.-P. et al. Global warming pattern formation: sea surface temperature and rainfall. *J. Clim.* **23**, 966–986 (2010).
37. Zhou, S., Huang, P., Xie, S.-P., Huang, G. & Wang, L. Varying contributions of fast and slow responses cause asymmetric tropical rainfall change between CO₂ ramp-up and ramp-down. *Sci. Bull.* **67**, 1702–1711 (2022).
38. Li, G. et al. Increasing ocean stratification over the past half-century. *Nat. Clim. Change* **10**, 1116–1123 (2020).
39. Morrison, A. K., Waugh, D. W., Hogg, A. M., Jones, D. C. & Abernathy, R. P. Ventilation of the Southern Ocean pycnocline. *Annu. Rev. Mar. Sci.* **14**, 405–430 (2022).
40. Shi, J.-R., Xie, S.-P. & Talley, L. D. Evolving relative importance of the Southern Ocean and North Atlantic in anthropogenic ocean heat uptake. *J. Clim.* **31**, 7459–7479 (2018).

41. Liu, W., Lu, J., Xie, S.-P. & Fedorov, A. Southern Ocean heat uptake, redistribution, and storage in a warming climate: the role of meridional overturning circulation. *J. Clim.* **31**, 4727–4743 (2018).
42. Huguenin, M. F., Holmes, R. M. & England, M. H. Drivers and distribution of global ocean heat uptake over the last half century. *Nat. Commun.* **13**, 4921 (2022).
43. An, S.-I. et al. General circulation and global heat transport in a quadrupling CO₂ pulse experiment. *Sci. Rep.* **12**, 11569 (2022).
44. Gregory, J. & Webb, M. Tropospheric adjustment induces a cloud component in CO₂ forcing. *J. Clim.* **21**, 58–71 (2008).
45. Bourgeois, T., Goris, N., Schwinger, J. & Tjiputra, J. F. Stratification constrains future heat and carbon uptake in the Southern Ocean between 30°S and 55°S. *Nat. Commun.* **13**, 340 (2022).
46. Bronselaer, B. & Zanna, L. Heat and carbon coupling reveals ocean warming due to circulation changes. *Nature* **584**, 227–233 (2020).
47. Gent, P. R. & Mcwilliams, J. C. Isopycnal mixing in ocean circulation models. *J. Phys. Oceanogr.* **20**, 150–155 (1990).
48. Wu, P., Jackson, L., Pardaens, A. & Schaller, N. Extended warming of the northern high latitudes due to an overshoot of the Atlantic meridional overturning circulation. *Geophys. Res. Lett.* **38**, L24704 (2011).
49. Redi, M. H. Oceanic isopycnal mixing by coordinate rotation. *J. Phys. Oceanogr.* **12**, 1154–1158 (1982).
50. Stuecker, M. F. et al. Polar amplification dominated by local forcing and feedbacks. *Nat. Clim. Change* **8**, 1076–1081 (2018).
51. Mechoso, C. R. et al. Can reducing the incoming energy flux over the Southern Ocean in a CGCM improve its simulation of tropical climate? *Geophys. Res. Lett.* **43**, 11,057–11,063 (2016).
52. Kim, H., Kang, S. M., Kay, J. E., Xie, S.-P. & Hartmann, D. Subtropical clouds key to Southern Ocean teleconnections to the tropical Pacific. *Proc. Natl Acad. Sci. USA* **119**, e2200514119 (2022).
53. Schneider, T., Bischoff, T. & Haug, G. H. Migrations and dynamics of the intertropical convergence zone. *Nature* **513**, 45–53 (2014).
54. Bischoff, T. & Schneider, T. Energetic constraints on the position of the intertropical convergence zone. *J. Clim.* **27**, 4937–4951 (2014).
55. White, R. H. et al. Tropical precipitation and cross-equatorial heat transport in response to localized heating: basin and hemisphere dependence. *Geophys. Res. Lett.* **45**, 11,949–11,958 (2018).
56. Byrne, M. P., Pendergrass, A. G., Rapp, A. D. & Wodzicki, K. R. Response of the intertropical convergence zone to climate change: location, width, and strength. *Curr. Clim. Change Rep.* **4**, 355–370 (2018).
57. Cai, W. et al. Increasing frequency of extreme El Niño events due to greenhouse warming. *Nat. Clim. Change* **4**, 111–116 (2014).
58. Hoskins, B. J. & Karoly, D. J. The steady linear response of a spherical atmosphere to thermal and orographic forcing. *J. Atmos. Sci.* **38**, 1179–1196 (1981).
59. Goosse, H. et al. Quantifying climate feedbacks in polar regions. *Nat. Commun.* **9**, 1919 (2018).

Publisher's note Springer Nature remains neutral with regard to jurisdictional claims in published maps and institutional affiliations.

Springer Nature or its licensor (e.g. a society or other partner) holds exclusive rights to this article under a publishing agreement with the author(s) or other rightsholder(s); author self-archiving of the accepted manuscript version of this article is solely governed by the terms of such publishing agreement and applicable law.

© The Author(s), under exclusive licence to Springer Nature Limited 2024

Methods

Dataset and experimental design

This study employed the Community Earth System Model v.1.2 (CESM1.2), which incorporates the Community Atmospheric Model v.5 (CAM5), Community Land Model v.4 (CLM4), the Community Ice Code v.4 (CICE4) and the Parallel Ocean v.2 (POP2). The CAM5 and CLM4 used a horizontal resolution of $\sim 1^\circ$, with 30 vertical levels. The CICE4 and POP2 used a nominal 1° horizontal resolution (the meridional resolution was $\sim 1/3^\circ$ near the equator), with 60 vertical ocean levels.

Two kinds of idealized climate model simulations were conducted. One was a present-day simulation with a constant atmospheric CO₂ concentration (present-day level, 367 ppm) integrated over 900 yr. The second was a CO₂ ramp-up and ramp-down simulation, and branched from the 28 different initial conditions in the present-day simulation. This experiment increased the atmospheric CO₂ concentration at a rate of 1% yr⁻¹ until it was quadrupled (1,468 ppm) over 140 yr, then symmetrically decreased CO₂ concentration at the same rate for 140 yr until it reached the initial value (367 ppm). Subsequently, a restoring experiment was conducted with a constant CO₂ concentration (367 ppm) for 220 yr, representing a net-zero emissions period. The total period for the second experiment was 500 yr, and it included 28 ensemble members. This experimental design is the same as that used by the 1pctCO₂-cdr scenario of the Carbon Dioxide Removal Model Intercomparison Project (CDRMIP)⁶⁰, except for the initial CO₂ level (pre-industrial level, 284.7 ppm).

We also used historical, 1pctCO₂ and 1pctCO₂-cdr scenarios based on 8 CMIP6 models: ACCESS-ESM1-5, CESM2, CNRM-ESM2-1, CanESM5, GFDL-ESM4, MIROC-ES2L, NorESM2-LM and UKESM1-0-LL. Each model of the 1pctCO₂-cdr scenario has a different length of restoring period prescribing constant CO₂ forcing: 620, 60, 60, 160, 60, 362, 119 and 510 yr, respectively. The CMIP6 dataset was used after re-gridding to $1^\circ \times 1^\circ$ horizontal resolution.

Design of the initial warming experiment

To explore the role of deep ocean warming in shaping the irreversible SST pattern, four kinds of initial warming experiments (named IW_whole, IW_be100, IW_be700 and IW_ab100) were carried out. All IW_EXPs were branched from the initial condition (year 2000) of each ensemble member and integrated with constant atmospheric CO₂ concentration (367 ppm), except that the horizontally uniform temperature anomaly profile was added to the initial ocean condition. The added temperature anomaly was the global mean potential temperature in the year 2280 when the CO₂ concentration first returned to its initial value (Fig. 3a). To prevent a potential imbalance of density, the salinity anomaly profile was also added to the initial ocean condition. That is, in all grids, the initial temperature and salinity perturbations were identical. Note that the initial warming was applied to the whole depth, below 100 m, below 700 m and above 100 m in the IW_whole, IW_be100, IW_be700 and IW_ab100 experiments, respectively, to isolate the deep ocean's intrinsic role. All IW_EXPs were integrated for 150 yr with 9 ensemble members, except that the IW_ab100 had 3 ensemble members.

Stratification metric

In this study, the ocean stratification (static stability) was measured as the squared buoyancy frequency (N^2):

$$N^2 = -g \frac{1}{\rho_0} \frac{\partial \rho}{\partial z}, \quad (1)$$

where g , ρ_0 and ρ are the seawater density, gravitational acceleration and potential density, respectively.

Data availability

The data used in this study are available from <https://doi.org/10.6084/m9.figshare.24873216.v1> (ref. 61), and the CMIP6 archives are freely available from <https://esgf-node.llnl.gov/projects/cmip6>.

Code availability

The codes used in this study are available from <https://doi.org/10.6084/m9.figshare.24873216.v1> (ref. 61). All figures were generated using Python with the matplotlib and basemap modules (<https://matplotlib.org/>, <https://matplotlib.org/basemap/>).

References

60. Keller, D. P. et al. The carbon dioxide removal model intercomparison project (CDRMIP): rationale and experimental protocol for CMIP6. *Geosci. Model Dev.* **11**, 1133–1160 (2018).
61. Oh, J.-H. Emergent climate change patterns originating from deep ocean warming in climate mitigation scenarios. figshare <https://doi.org/10.6084/m9.figshare.24873216.v1> (2023).

Acknowledgements

The CESM simulation and data transfer were supported by the National Supercomputing Center with supercomputing resources (KSC-2023-CHA-0001), and the National Center for Meteorological Supercomputer of the Korea Meteorological Administration (KMA) and the Korea Research Environment Open NETwork (KREONET), respectively. J.-S.K. was supported by a National Research Foundation of Korea (NRF) grant funded by the Korean government (NRF-2022R1A3B1077622). S.-I.A. was supported by the National Research Foundation of Korea (NRF-2018R1A5A1024958). This is PMEL contribution no. 5451.

Author contributions

J.-H.O. compiled the data, conducted analyses and simulations, prepared the figures and wrote the paper. J.-S.K. designed the research and wrote the paper. All authors discussed the results and revised the paper.

Competing interests

The authors declare no competing interests.

Additional information

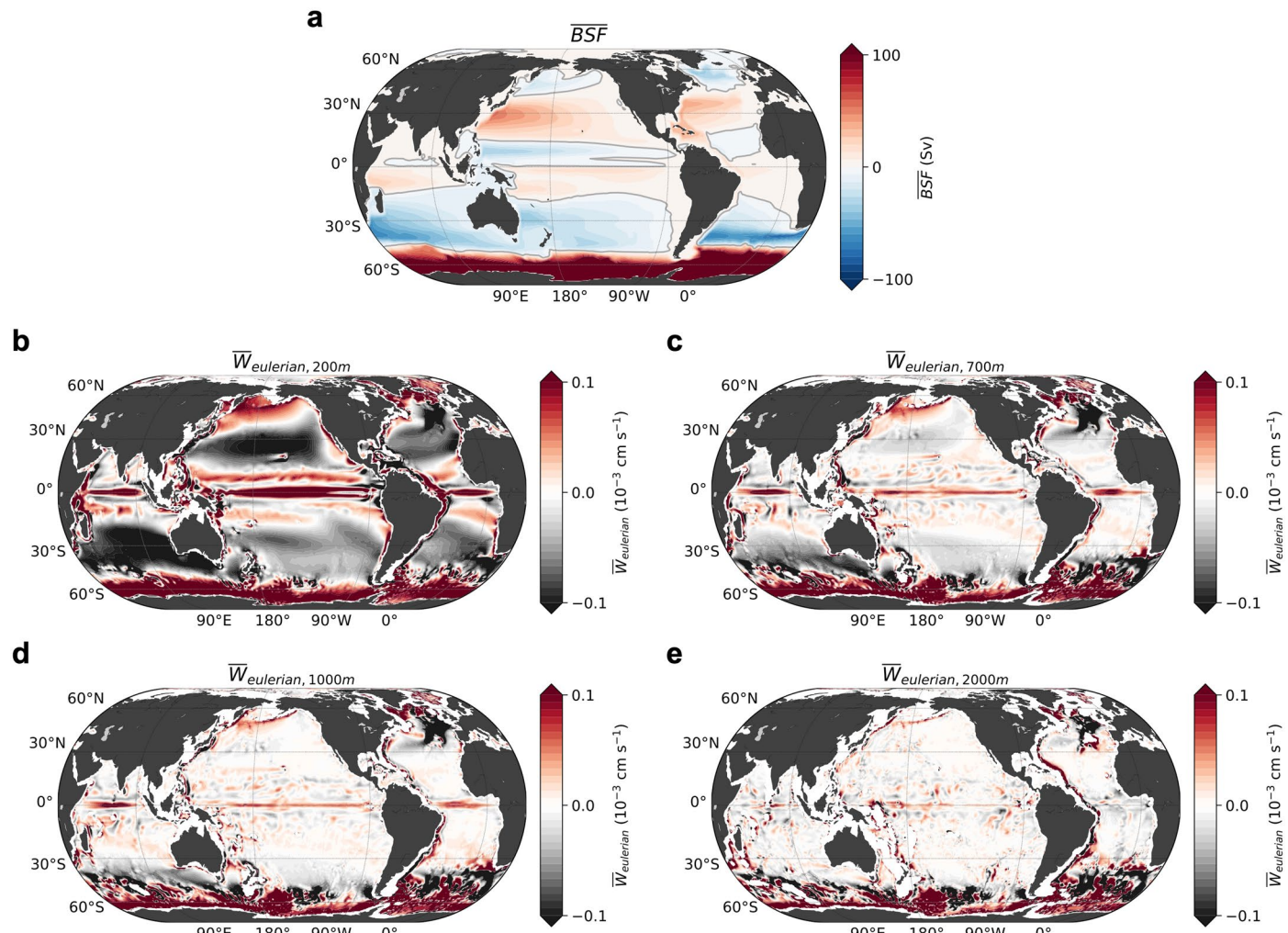
Extended data is available for this paper at <https://doi.org/10.1038/s41558-024-01928-0>.

Supplementary information The online version contains supplementary material available at <https://doi.org/10.1038/s41558-024-01928-0>.

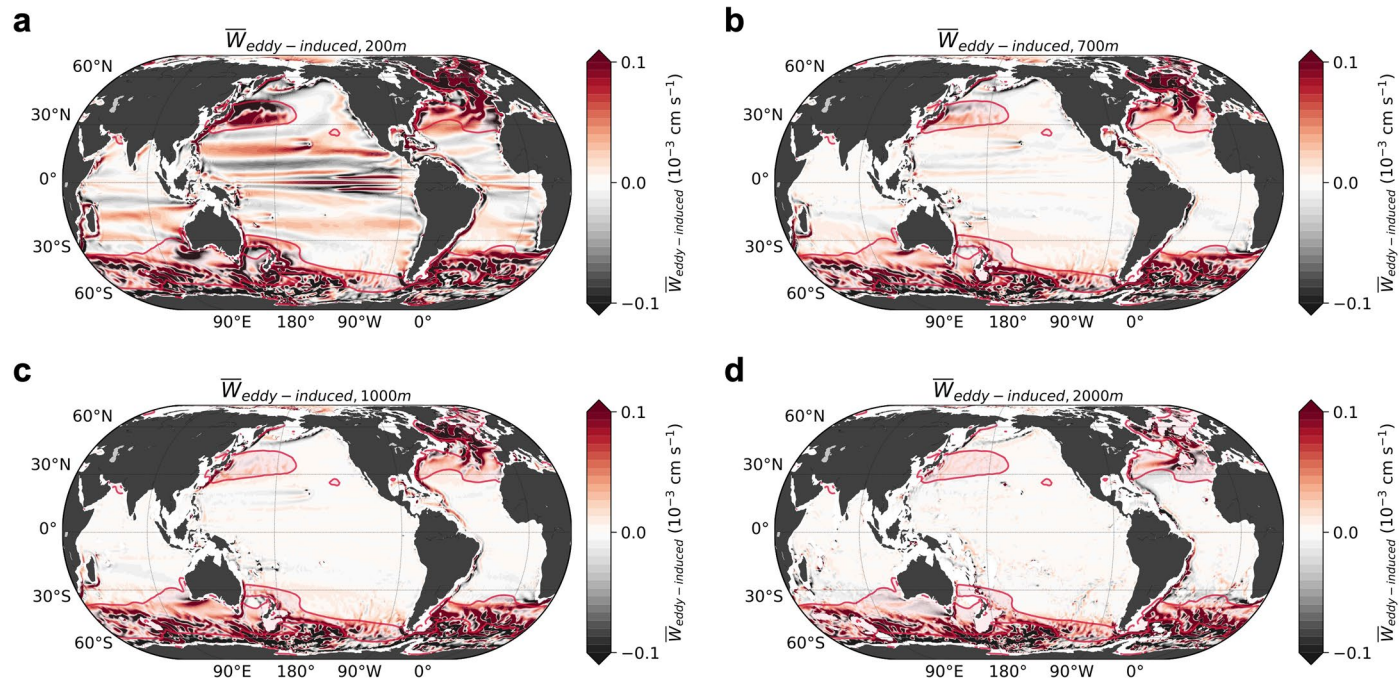
Correspondence and requests for materials should be addressed to Jong-Seong Kug.

Peer review information *Nature Climate Change* thanks George Nurser, Kirsten Zickfeld and the other, anonymous, reviewer(s) for their contribution to the peer review of this work.

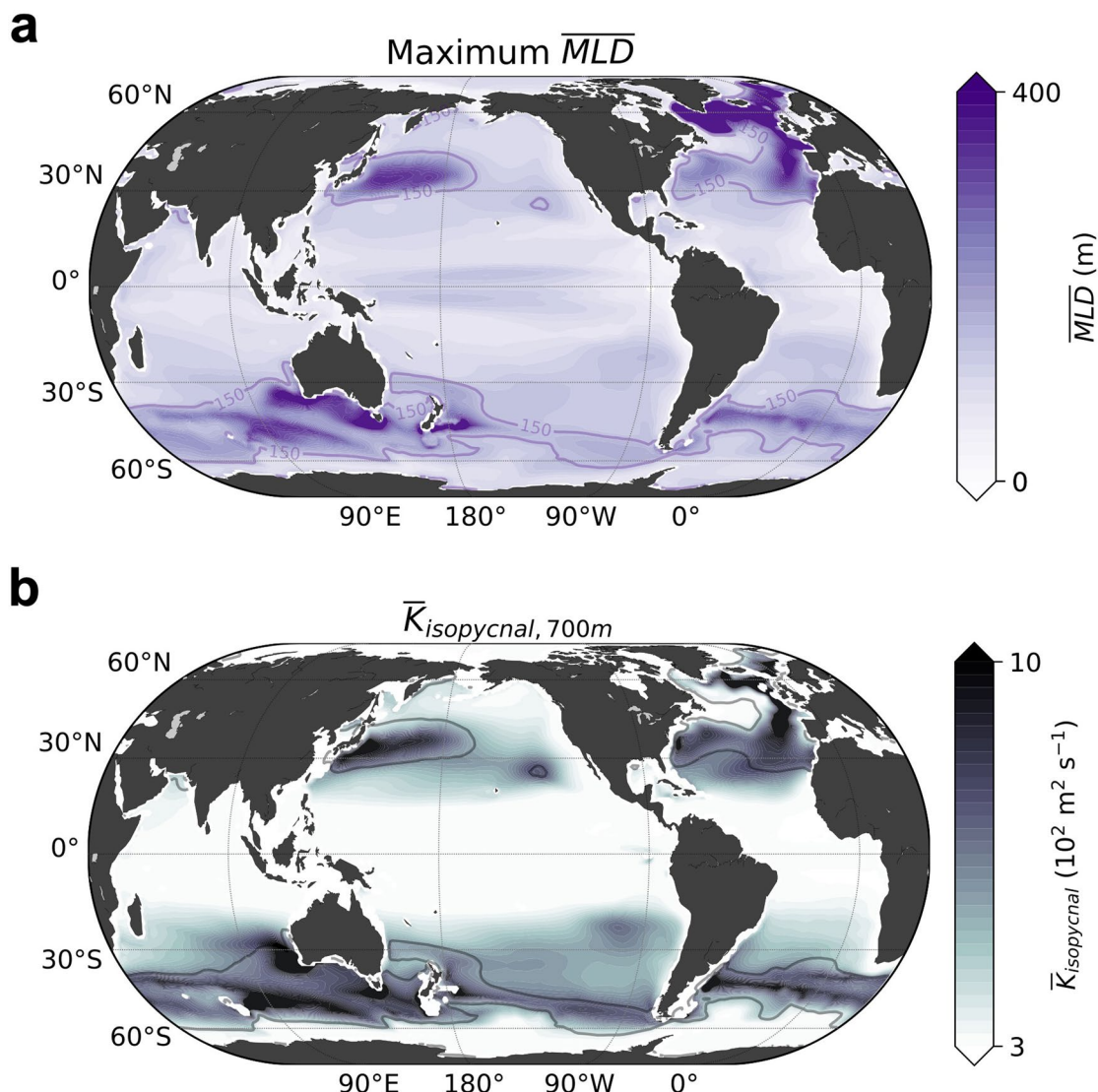
Reprints and permissions information is available at www.nature.com/reprints.



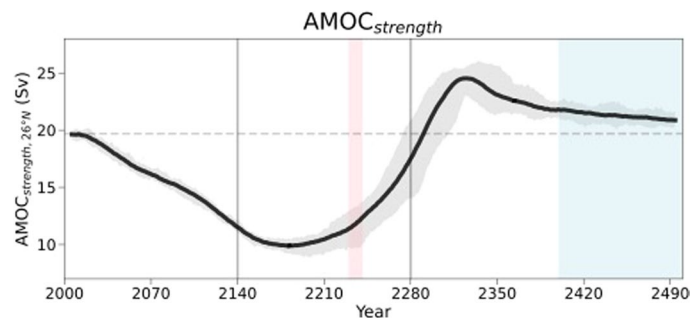
Extended Data Fig. 1 | Background barotropic stream function and Eulerian vertical velocity. **a**, Background annual mean barotropic stream function. The black line indicates the barotropic stream function of 0 Sv. **b, c, d, e**, Background annual mean Eulerian vertical velocity ($\overline{W}_{eulerian}$) at 200 m, 700 m, 1000 m, and 2000 m, respectively.



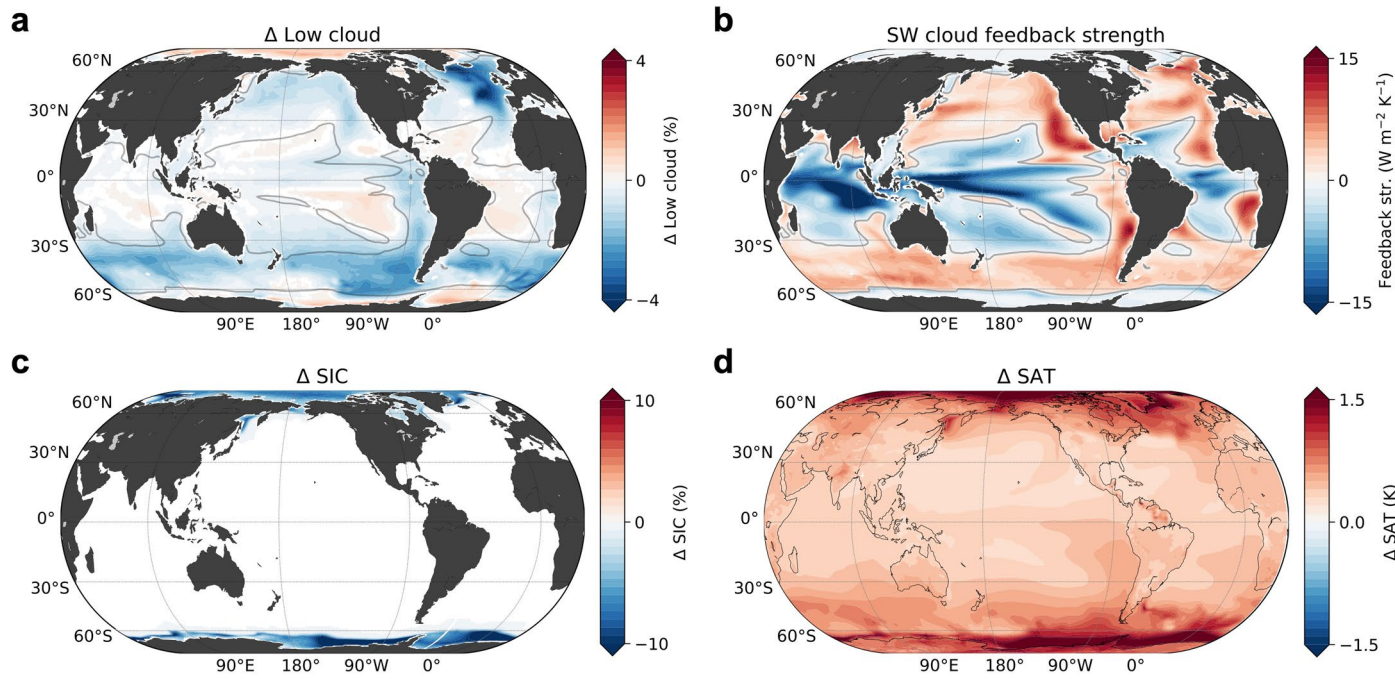
Extended Data Fig. 2 | Background eddy-induced vertical velocity. a, b, c, d. As in Extended Data Fig. 1, but for the eddy-induced vertical velocity ($\bar{W}_{\text{eddy-induced}}$, bolus vertical velocity). The red contour denotes the maximum mixed layer depth of 150 m (see Extended Data Fig. 3a).



Extended Data Fig. 3 | Background maximum mixed layer depth (MMLD) and isopycnal diffusivity. **a, b,** Maximum mixed layer depth (monthly maximum among 12 months climatology in each grid) and isopycnal diffusivity at 700 m for the CESM1 (present-day control simulation, see Methods). The contour in panels a and b indicates the MMLD of 150 m.

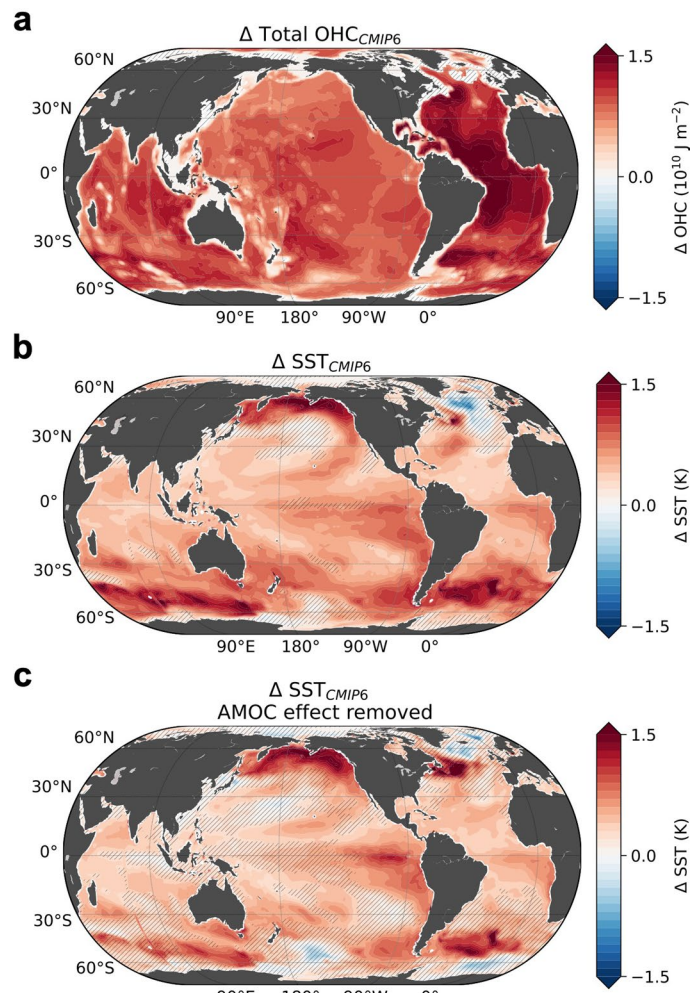


Extended Data Fig. 4 | Temporal evolution of the changes in AMOC strength. Temporal evolution of the AMOC strength defined as the maximum of the ocean stream function below 500 m at 26°N. The line and shading are as in Fig. 1a.



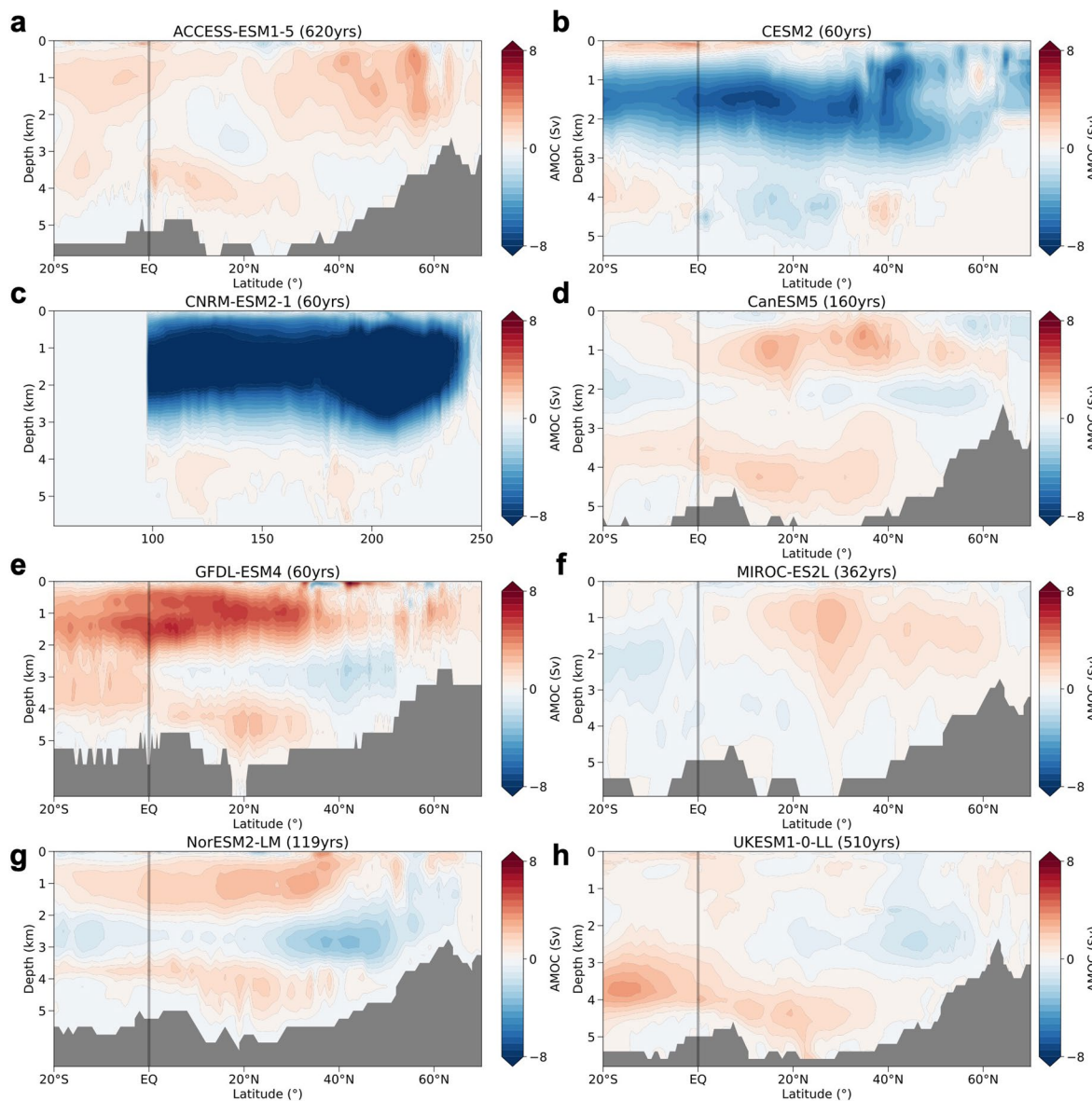
Extended Data Fig. 5 | Positive feedbacks amplifying the irreversible SST warming. **a, c, d.** As in Fig. 2a, but for the low cloud fraction, sea ice concentration, and surface air temperature, respectively. **b.** Shortwave cloud feedback strength (SWCFS) in the present-day control simulation, which is calculated as shortwave radiation at the top of the atmosphere regressed onto the underlying SST at each grid. The positive feedback between the SST and low clouds (that is shortwave cloud feedback) can amplify the irreversible SST warming: As the amount of low clouds decreases, the amount of solar radiation

reaching the surface increases, resulting in a warming effect on the local SST. This SST warming, in turn, decreases atmospheric stability, which subsequently contributes to a decrease in the amount of low clouds. The black contour in panel **a** and **b** indicates the SWCFS of $0 \text{ W m}^{-2} \text{ K}^{-1}$. It is clear that the significant reduction in low cloud fraction occurs in regions with strong cloud feedback in the present climate. This low cloud reduction pattern well explains the distribution of the surface air temperature anomaly with significant sea-ice reduction in polar oceans, indicating the positive local feedbacks.

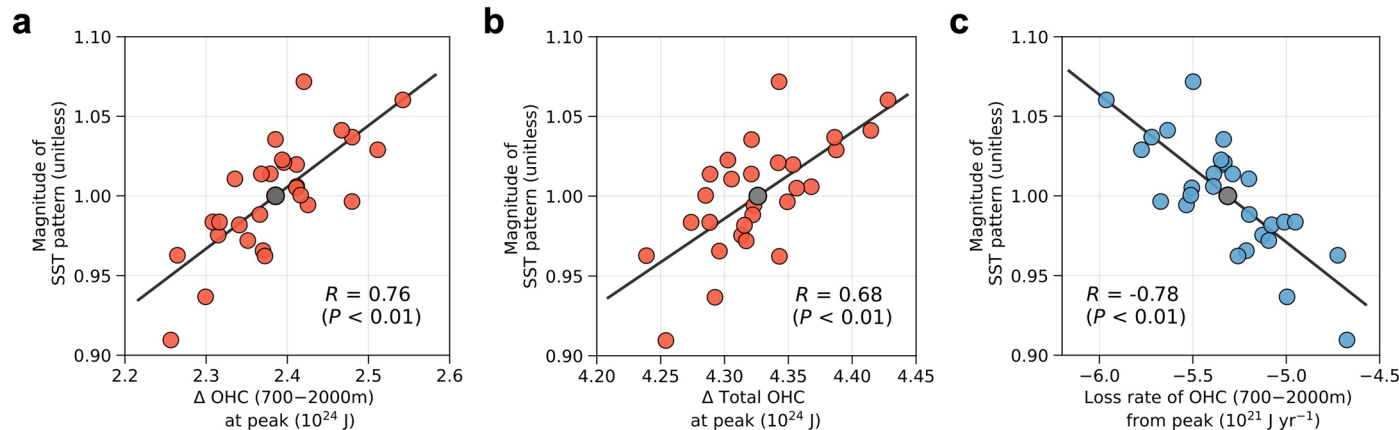


Extended Data Fig. 6 | Spatial patterns of the irreversible OHC and SST changes in CMIP6 models. a, b, Multi-model mean in the total OHC and SST anomalies averaged over the restoring period of each CMIP6 model ACCESS-ESM1-5, CESM2, CNRM-ESM2-1, CanESM5, GFDL-ESM4, MIROC-ES2L,

NorESM2-LM, UKESM1-0-LL). c, Same as in b, but the AMOC effect is linearly removed using simple linear regression between AMOC strength and SST field. Note that the length of restoring period in each CMIP6 model is different (see Methods). Hatchings indicate insignificant responses at the 95% confidence level.

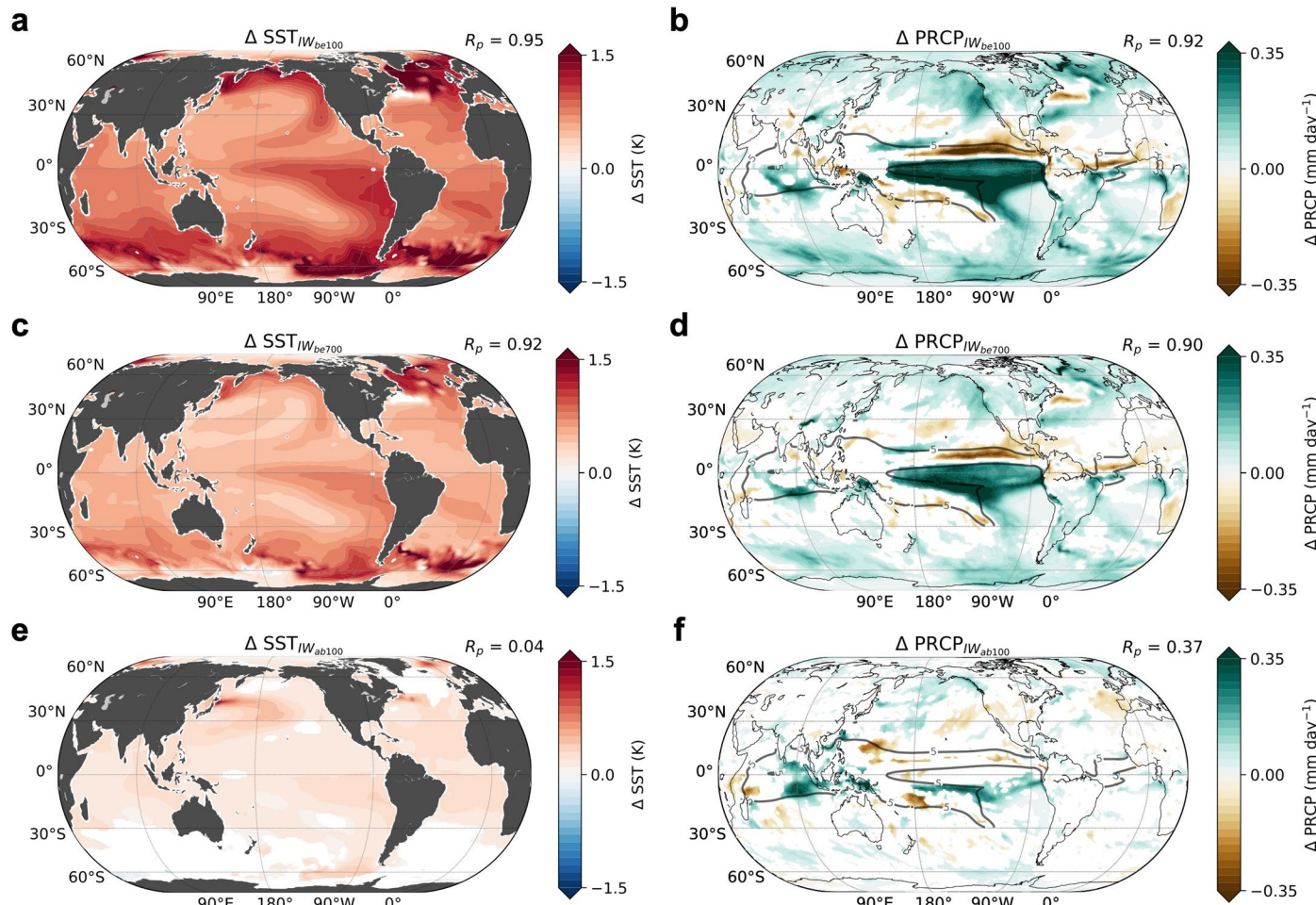


Extended Data Fig. 7 | Patterns of the AMOC changes in CMIP6 models. **a, b, c, d, e, f, g, h,** AMOC anomalies averaged over the restoring period of each CMIP6 model ACCESS-ESM1-5, CESM2, CNRM-ESM2-1, CanESM5, GFDL-ESM4, MIROC-ES2L, NorESM2-LM, UKESM1-0-LL.



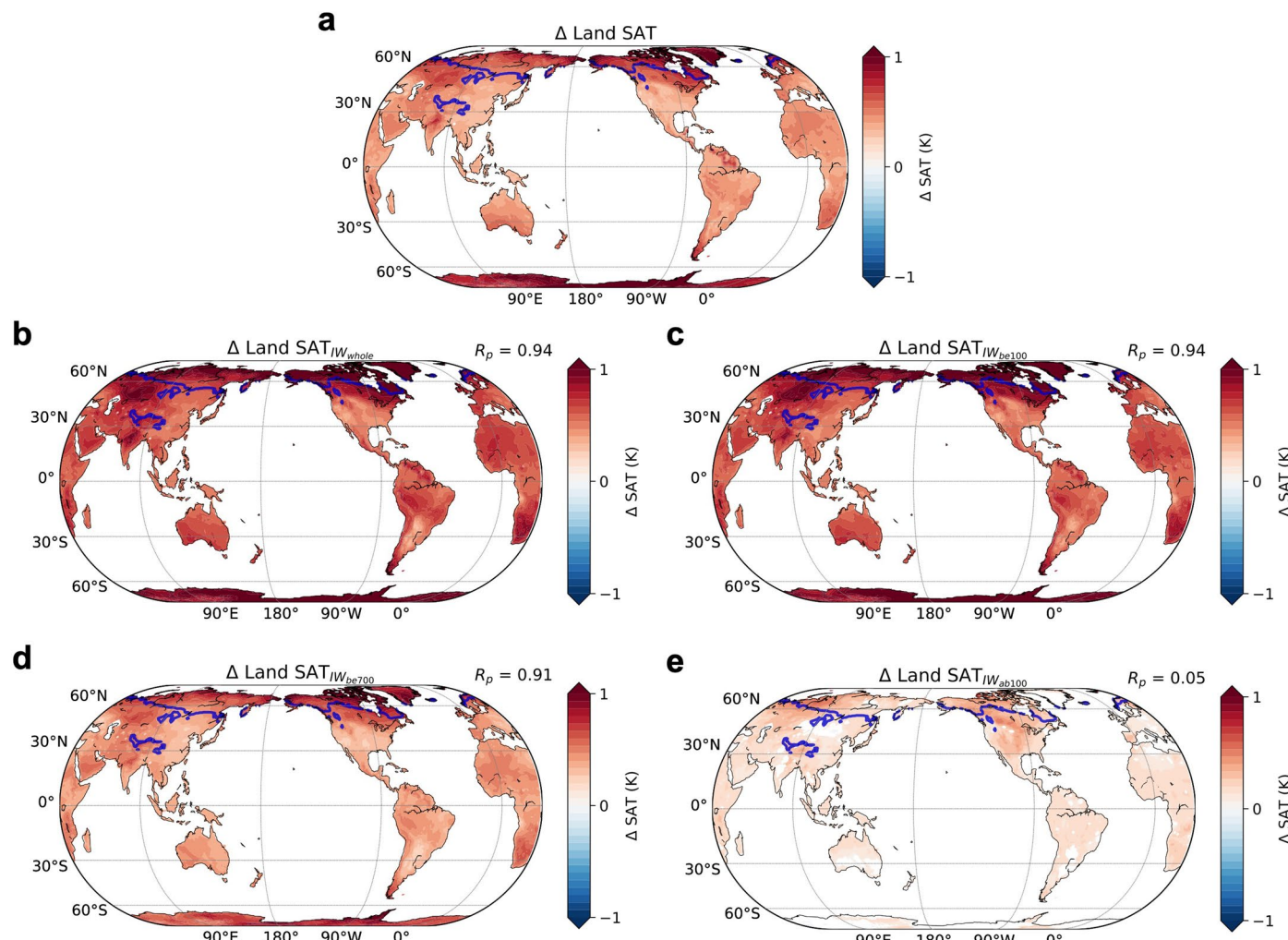
Extended Data Fig. 8 | Inter-ensemble relationship between global OHC and irreversible SST pattern. **a**, Magnitude of irreversible SST pattern (see Methods) against global total OHC anomaly at its peak for each of 28 ensemble members. The gray dot indicates the ensemble mean. **b**, As in panel **a**, but for global

700–2000 m integrated OHC anomaly. **c**, As in panel **a**, but for 700–2000 m integrated OHC from its peak. The p value based on two-sided student's t test in each panel is 7.2×10^{-5} , 3.3×10^{-6} , and 9.3×10^{-7} , respectively.



Extended Data Fig. 9 | Spatial patterns of the irreversible surface climate changes in initial warming experiments. **a, b**, As in Fig. 3c, d, but for the IW_be100. **c, d**, As in Fig. 4c, d, but for the IW_be700. **e, f**, As in Fig. 3c, d, but for the IW_up100. Only significant values at the 95% confidence level are shown in

all panels. The numbers labeled at the upper top corner in panels are the pattern correlations between each panel's pattern and the reference irreversible SST and PRCP patterns (Figs. 2a and 2d).



Extended Data Fig. 10 | Spatial patterns of the irreversible land temperature changes. **a**, As in Fig. 2a, but for the land surface air temperature (SAT). **b, c, d, e**, As in Fig. 3c, but for the land SAT in IW_{total}, IW_{be100}, IW_{be700}, and IW_{up100}, respectively. The blue lines in each panel show the climatological annual mean

snow cover edge of 50% in the present-day simulation. Only significant values at the 95% confidence level are shown in all panels. The numbers labeled at the upper top corner in panels (b–e) are the pattern correlations between each panel's pattern and the pattern in panel **a**.